The Astrophysical Journal, 950:144 (10pp), 2023 June 20 https://doi.org/10.3847/1538-4357/accf9f

Magnetic Reconnection Rate in the M6.5 Solar Flare on 2015 June 22

Bryce Cannon[1], Ju Jing[1,2], Qin Li[1,2], Nian Liu[1,2], Jeongwoo Lee[1,2], Wenda Cao[1,2], and Haimin Wang[1,2]
[1] Institute for Space Weather Sciences, New Jersey Institute of Technology, University Heights, Newark, NJ 07102-1982, USA; ju.jing@njit.edu
[2] Big Bear Solar Observatory, New Jersey Institute of Technology, 40386 North Shore Lane, Big Bear City, CA 92314-9672, USA
Received 2022 October 5; revised 2023 April 21; accepted 2023 April 21; published 2023 June 19

Abstract

Magnetic reconnection is regarded as the mechanism for the rapid release of magnetic energy stored in active regions during solar flares, and quantitative measurements of the magnetic reconnection rate are essential for understanding solar flares. In the context of the standard two-ribbon flare model, we derive the coronal magnetic reconnection rate of the M6.5 flare on 2015 June 22 in two terms, reconnection flux change rate and reconnection electric field, both of which can be obtained from observations of the flare morphology. Data used include a sequence of chromospheric Hα images with unprecedented resolution during the flare from the Visual Imaging Spectrometer of the Goode Solar Telescope (GST) at the Big Bear Solar Observatory and a preflare line-of-sight photospheric magnetogram from the GST Near-InfraRed Imaging Spectropolarimeter along with hard X-ray data from the Ramaty High Energy Solar Spectroscopic Imager. The temporal correlation between the magnetic reconnection rate and nonthermal emission is found, and the variation of the reconnection electric field is mainly determined by the ribbon speed, not by the local magnetic field encountered by the ribbon front. Spatially, the hard X-ray source overlaps with the location of the strongest electric field obtained at the same time. The ribbon motion shows abundant fine structures, including a local acceleration at the location of a light bridge with a weaker magnetic field.

Unified Astronomy Thesaurus concepts: Solar flares (1496); Solar magnetic reconnection (1504)

Supporting material: animation

1. Introduction

Magnetic reconnection is an important process in highly conducting plasma in which free magnetic energy is quickly converted into other forms of energy, such as kinetic energy, thermal energy, and nonthermal particle acceleration. Observations of solar two-ribbon flares provide an opportunity to determine the magnetic reconnection rate. Specifically, during the process of a flare, the enhanced emission of the two ribbons forms on either side of the polarity inversion line (PIL) at the chromosphere in response to the precipitation of nonthermal particles accelerated by magnetic reconnection in the corona. The separation motion of the two ribbons tracks the chromospheric footpoints of newly reconnected field lines, and hence enables an indirect measurement of coronal magnetic reconnection from lower-atmosphere flare ribbon observations. The relationship between the observed flare ribbons and the coronal magnetic reconnection geometry is schematically demonstrated by the standard two-ribbon flare model, also known as the CSHKP model (Carmichael 1964; Sturrock 1966; Hirayama 1974; Kopp & Pneuman 1976).

The standard model is a two-dimensional (2D) model with an X-point reconnection. In this model, there are two related proxies for the reconnection rate: the electric field E associated with the 2D reconnection at the X-point, and the reconnection flux change rate $\dot{\Phi}$. The two measures of reconnection are proportional and differ by the length along the third dimension (i.e., along the ribbon). Specifically, E is originally defined as $E = v_{\rm in}B_{\rm c}$, where $v_{\rm in}$ and $B_{\rm c}$ are the inflow velocity and strength of the inflow magnetic field to the reconnection X-point in the corona, respectively (Forbes & Priest 1984). However, neither of these quantities can be measured directly from observations. Since the reconnecting magnetic field lines at the reconnection site are tied down to those swept by the ribbon motion at the lower atmosphere, the calculation of E can be replaced by the following:

$$E = v_{\rm rib}B_z. \quad (1)$$

Here, $v_{\rm rib}$ is the apparent separation velocity of the flare ribbon seen in the chromospheric Hα observations, and B_z is the vertical component of the magnetic field at the ribbon location (Forbes & Priest 1984). We assume that the B_z field in the chromosphere is not so different from the B_z field in the photosphere that is directly accessible from photospheric magnetogram data, so that both $v_{\rm rib}$ and B_z are observable quantities. Similarly, under the line-tying assumption and the three-dimensional (3D) generalizations of the standard model, the reconnection flux change rate $\dot{\Phi}$ can be calculated by the rate of magnetic flux swept by the flare ribbon, i.e.,

$$\dot{\Phi} = \frac{d}{dt}\int B_z da, \quad (2)$$

where da is the newly brightened area of the flare ribbon. Thus, both E and $\dot{\Phi}$ can be derived from observations.

The establishment of the above two equations has led to remarkable progress in the study of magnetic reconnection in solar flares over the past two decades (see the review by Lee 2015). The reconnection flux database has been built on this basis (Kazachenko et al. 2017). Some of the most significant results include: (1) the temporal correlation between the reconnection rate and nonthermal hard X-ray (HXR) lightcurves (e.g., Qiu et al. 2002, 2004, 2010; Lee et al. 2006);

(2) a statistically positive correlation between the reconnection rate and the acceleration of coronal mass ejections (CMEs) at the early phase of the eruptions (Jing et al. 2005; Zhu et al. 2020); and (3) a statistically negative correlation between the reconnection rate and the HXR spectral index (Liu et al. 2007). These studies have mainly focused on the temporal properties of E and $\dot{\Phi}$ and their statistical correlation with CMEs, while relatively few studies have investigated the spatial properties of reconnection rates.

Among the few such studies, Jing et al. (2008) found that the location of the G-band kernel representing nonthermal emission spatially coincides with that of the strongest reconnection rate. It is also worth mentioning that an empirical relationship between the two contributing factors of E, $v_{\rm rib}$ and B_z, is found at the flare peak time, i.e., $v_{\rm rib} \propto B_z^{-0.15}$. This means that the ribbon velocity is slower in the strong-field region than it is in the weak-field region (Jing et al. 2008). Likewise, neither $v_{\rm rib}$ nor B_z is uniformly distributed along the ribbon, and therefore E should also vary along the ribbon. However, we expect that the inverse relationship between $v_{\rm rib}$ and B_z may reduce the spatial variation of E along the ribbon to some extent.

Variation of $v_{\rm rib}$ along a ribbon may indicate that the corresponding coronal reconnection region has a nonuniform structure along the X-line. Recently, there is increasing evidence from simulations (e.g., Wyper & Pontin 2014, 2021) that reconnection within the coronal reconnecting current sheet is inherently intermittent and fragmented, perhaps due to tearing instability. Flare ribbons, as projections of the coronal reconnection process on the surface, also provide indirect evidence for this bursty nature of reconnection, such as the sawtooth substructure in the ribbon section (Brannon et al. 2015), and the highly structured ribbon front in both space and time (Naus et al. 2022).

There is no doubt that determining the spatiotemporal dynamical behavior of flare ribbons is essential for understanding the coronal magnetic reconnection process. However, such a study requires observational data with sufficient spatial and temporal resolution. This study takes advantage of the exceptionally high-resolution observation of the M6.5 flare (SOL2015-06-22T18:23) taken by the 1.6 m Goode Solar Telescope (GST; Goode & Cao 2012) at the Big Bear Solar Observatory (BBSO). This GST data set of the flare, with its high resolution and complete coverage of the flare process, has facilitated a large number of in-depth studies of the flare (Jing et al. 2016; Liu et al. 2016; Wang et al. 2017; Xu et al. 2018; Wang et al. 2018; Huang et al. 2019). Another particular advantage of this observation is that the region passed through by one of the flare ribbons includes two sunspots and a well-resolved light bridge (LB) between them. This allows us to study the velocity of the ribbon over the different magnetic field regions, and thus to gain a quantitative understanding of the $v_{\rm rib}$–B_z relationship and the inhomogeneity of the reconnection rate.

2. GST Data

The flare took place on 2015 June 22 in NOAA Active Region (AR) 12371, then near the center of the solar disk (129″, 168″), and was associated with a subsequent halo CME. To derive the magnetic reconnection rate of the flare, a sequence of Hα images and a preflare (17:34:03 UT) photospheric magnetogram are used in this study, assuming that the magnetic field does not change much over the course of the flare. These two data are obtained from the Visual Imaging Spectrometer (VIS; Cao et al. 2010) and Near-InfraRed Imaging Spectropolarimeter (NIRIS; Cao et al. 2012) of the GST, respectively. During the GST observation period of the flare, seeing was consistently good. In addition, the GST is equipped with a high-order adaptive optics system, which is used to stabilize the wave front aberrations caused by the atmospheric turbulence.

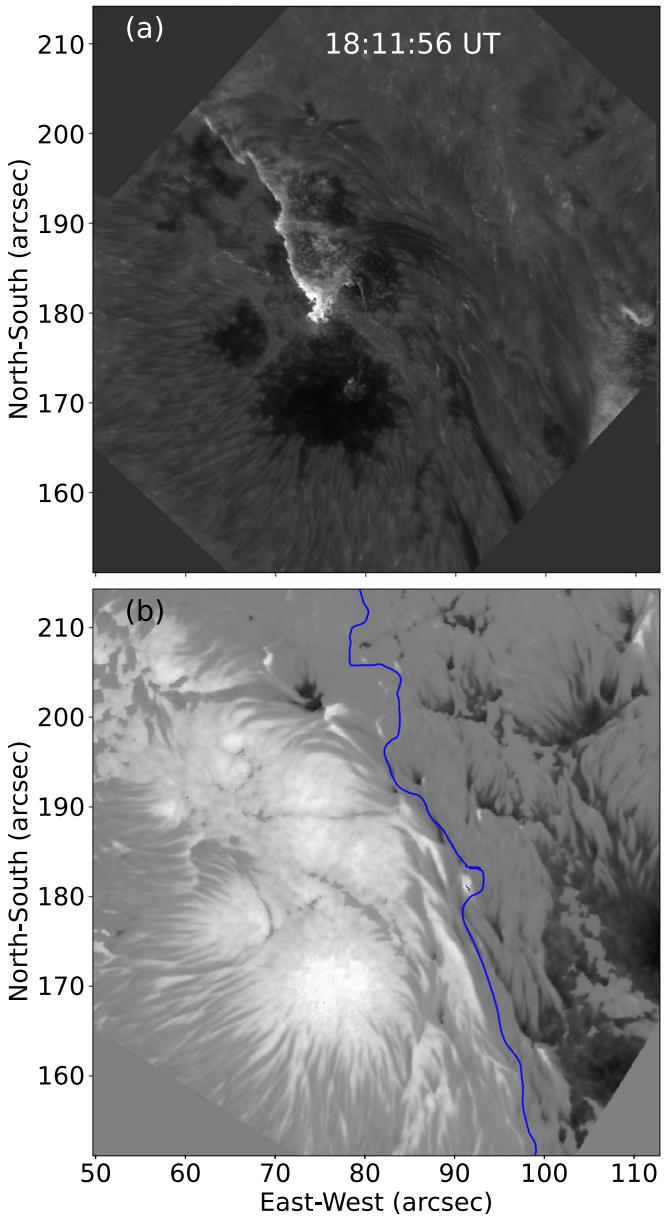

Figure 1. (a) Snapshot of the eastward moving ribbon of the flare, taken at 18:11:56 UT on 2015 June 22, by the GST in Hα. (b) GST longitudinal magnetogram, taken at 17:34:03 UT on the same day, 5 minutes prior to the flare onset. The blue contour shows the major magnetic PIL.

In particular, we used the Hα+1 Å image sequence throughout the entire process of the flare (17:39–18:51 UT) to track the ribbon motion (see Section 3 for details). The spatial sampling of these images is ∼0.″09 per pixel, and the average cadence is 28 s. The NIRIS photospheric magnetogram at the Fe I 1564.8 nm line is processed with the BBSO NIRIS data processing pipeline (Ahn et al. 2016; Ahn & Cao 2017), including dark- and flat-field corrections, instrument crosstalk

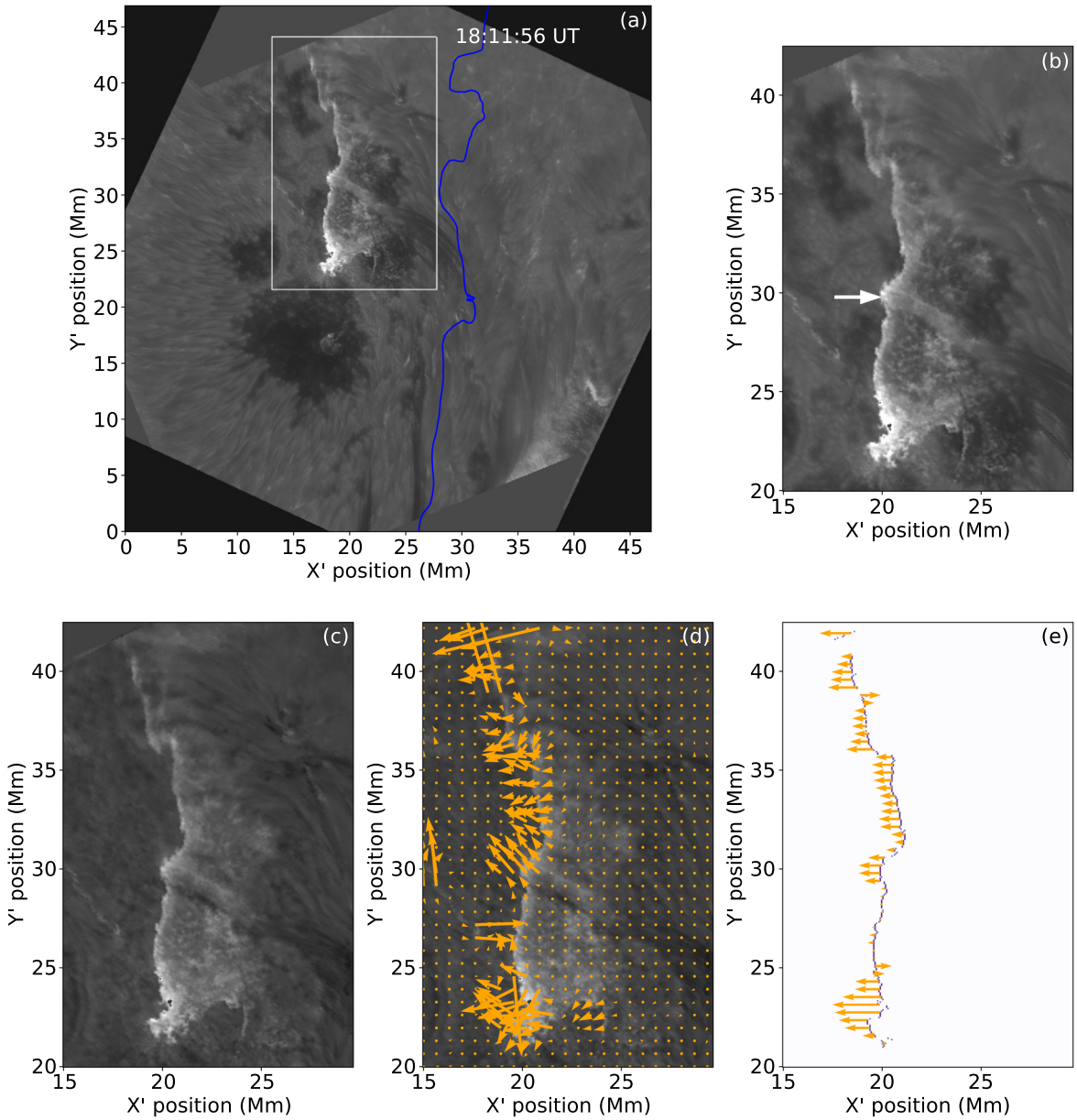

Figure 2. (a) Hα image taken at 18:11:56 UT, rotated clockwise 25°. The rectangle marks the field of view of panels (b)–(e) and Figures 4(a)–(b). The PIL is marked by the blue contour. (b) The zoomed-in Hα image. The arrow indicates the ribbon front passing through the LB, forming a wavelike structure. (c) The zoomed-in Hα image after subtracting a preflare frame (17:39:52 UT). (d) The velocity field calculated by the LCT algorithm overlaid on (c). (e) The detected leading edge of the ribbon and velocity vectors $v_{x'}$ along it. $v_{x'}$ serves as a proxy for $v_{\rm rib}$. An animation is available that shows the LCT velocity vectors superimposed with the Hα image sequence (left) and the longitudinal magnetogram at 17:34 UT (right). The start and stop times of the animation are 17:51:14 UT and 18:29:01 UT, respectively, and the duration of the video is 3 s.

(An animation of this figure is available.)

calibration, and Stokes inversion with the Milne–Eddington technique. The 180° azimuthal ambiguity of the vector magnetogram data was resolved using the ME0 code (Leka et al. 2009) based on the "minimum energy" algorithm (Metcalf 1994; Metcalf et al. 2006). The projection effect, although small because the AR is near the center of the disk, was corrected by transforming the observed vector fields to heliographic coordinates (Gary & Hagyard 1990). The preflare magnetogram used in this study was taken at 17:34:03 UT, 5 minutes before the flare onset, with a spatial sampling of $\sim$0.″078 per pixel.

Figure 1 shows a snapshot of the Hα image and the preflare magnetogram B_z. The two images were coaligned with subpixel precision. The flare is a typical two-ribbon flare. However, the field of view (FOV) of the GST data covers mainly the eastern part of the AR with positive magnetic polarity and the progression of the eastern ribbon over this field, so we limit our analysis to the eastern ribbon. The narrow sunspot LBs with weaker magnetic fields divide the sunspot into multiple parts, one of which is right in the path of the ribbon. We note that as the ribbon enters and leaves the LB, the part of the ribbon front near the LB moves faster than the other parts (see the movie in Jing et al. 2016), which seems to be consistent with the negative correlation between $v_{\rm rib}$ and B_z found by Jing et al. (2008). This inhomogeneity in the velocity of the ribbon front shows a fine structure in the form of wavy disturbances.

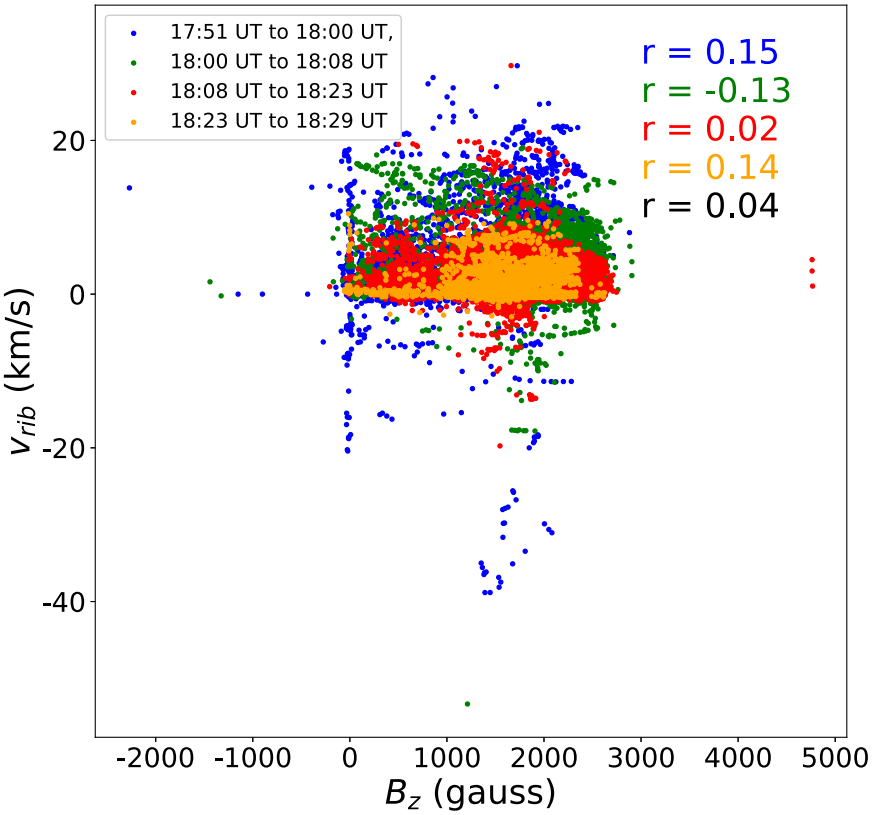

Figure 3. Scatterplot of $v_{\rm rib}$ vs. B_z, including all points along the leading edge of the ribbon over the period from 17:51:14 UT to 18:29:29 UT. This time period is divided into four time slots, and the $v_{\rm rib}$–B_z data pairs in each time slot are presented in four different colors, as shown in the inset. The overall correlation coefficient r and the correlation coefficients of the four subgroups are given in this figure.

3. Methods

We need to track the motion of the ribbon, together with its magnetic field, to derive the reconnection rate. Consistent with the standard model, we use only the leading edge of the expansion ribbon and the velocity component perpendicular to the PIL. As shown in Figure 1, the flare ribbon moves mainly to the east at a diagonal angle. Before we applied the local correlation tracking (LCT; Fisher & Welsch 2008) to the time sequence of Hα images to derive the velocity field, we did the following processing of the Hα images to optimize the LCT results and to simplify the later analysis. First, the images were rotated 25° clockwise around the image center, so that the ribbon moves in an essentially horizontal direction. The purpose of this is that the $v_{\rm rib}$ needed to calculate E is the ribbon velocity component perpendicular to the magnetic PIL. By rotating the image in this way, the $v_{x'}$ obtained from the LCT method afterwards is approximately $v_{\rm rib}$. Second, all the images were cropped to a smaller size highlighting the ribbon, so that the later LCT computation can be performed more quickly. Third, the ribbon was enhanced from the background by subtracting a preflare Hα image (taken at 17:39:52 UT) from each image. An example of such Hα image processing is shown in Figures 2(a)–(c). The axes of x' and y' are used to represent the axes after rotation, and the units are megameters for calculation purposes.

Then, the LCT method, pyflct available in Python, was applied to the processed images to obtain the velocity field. The LCT is performed by windowing the input image to isolate the features of interest, then computing the correlation function between the two images and tracking features by locating the peaks of the cross-correlation function (Fisher & Welsch 2008). Before calculating the correlation at a specific pixel, a Gaussian is used as a window to attenuate any correlation that is distant. This is where the "local" comes into local correlation tracking. In this study, we opted for a window size of 0.98×0.98 Mm^2, which is large enough to see large changes in ribbon position while balancing the run time of the LCT computation. Considering that the average cadence of the Hα data is 28 s, the velocity is limited to a maximum of 0.98 Mm/28 s = 35 km s^{-1}, whereas detection of higher speeds may be possible with higher cadence data (Lee et al. 2006). In fact, the ribbon movement in this event rarely reaches such a fast speed, as seen in Figure 3. An example of the velocity field calculated by LCT is shown in Figure 2(d), and an animation including all the velocity fields is available.

Once the velocity field is calculated, we are only interested in its x' component, because this component can be approximated as the ribbon separation velocity $v_{\rm rib}$. We next use the Canny edge detection algorithm (Xu et al. 2017) to pick out the pixels that serve as the leading edge of the moving ribbon, which is where energy flux from the corona deposit along the newly reconnected field lines. Some edges in dim areas (e.g., edges at the edge of the field of view) are irrelevant. To eliminate these, we only keep the edges with intensities greater than $\bar{I} + \frac{1}{2}\sigma$. $\bar{I}$ and σ are the average and standard deviation of Hα intensities, respectively, calculated over the field of view during the period from 17:51 UT to 18:29 UT. To find the leading edge of the ribbon, only the leftmost edge is kept, as shown in Figure 2(e). This edge detection does not always work perfectly. Sometimes the ribbon is too concave to detect the leading pixels well, and at other times, the

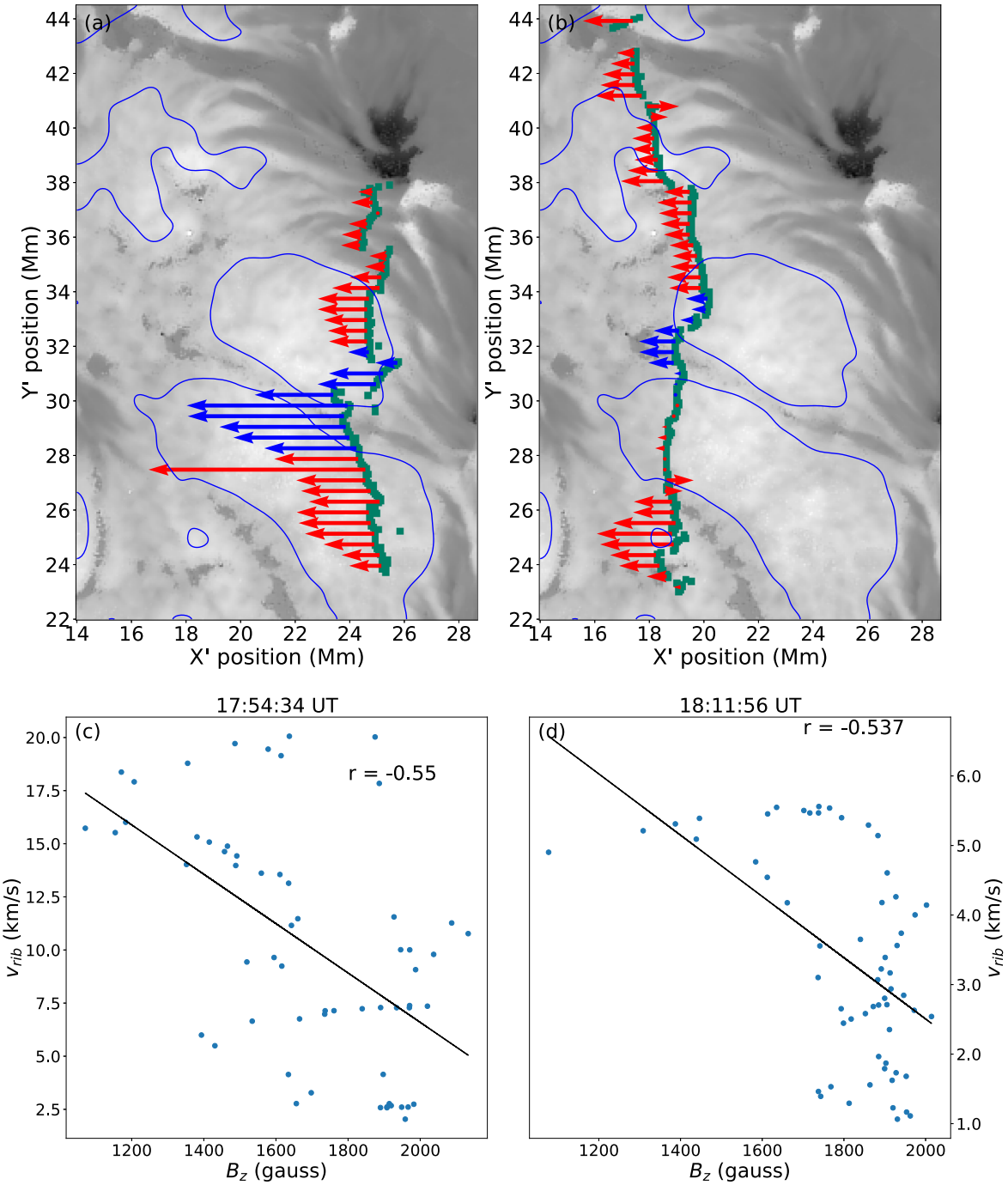

Figure 4. (a) The magnetogram taken at 17:54:04 UT, overlaid with the leading edge of the ribbon and the vectors of v_x along it. Note the increased velocity near the light bridge. The blue arrows represent the v_x vectors through and around the light bridge, distinguished from the v_x vectors far away from the light bridge (red arrows). The blue contours are the 48% maximum of the smoothed GST Hα intensity (taken at 17:36 UT) to outline the sunspots. (b) Same as (a), but at 18:11:56 UT. (c) Scatterplot of $v_{\rm rib}$ vs. B_z at 17:54:34 UT. The data points are from the leading edge segment through and around the light bridge (segments with blue arrows). (d) Same as (c), but at 18:11:56 UT when the ribbon is leaving the light bridge region.

leading edge is not prominent enough or bright enough to be picked up by the Canny edge detection algorithm. Apart from these imperfections, we now have the position of the leading edge at each moment during the travel of the ribbon, and the velocity of each point at these positions.

4. Analysis and Results

As mentioned earlier, the segment of the ribbon on the LB with a weaker magnetic field is faster, while the segment on the sunspots with a stronger magnetic field is slower. We attempt to find if there is really any correlation between $v_{\rm vib}$ and B_z. Figure 3 shows the scatterplot of $v_{\rm rib}$ versus B_z. Each data pair corresponds to a point at the magnetogram encountered by the leading edge of the ribbon during the flare process (from 17:51:14 UT to 18:29:29 UT). The values of $v_{\rm rib}$ and B_z are read from the point in the velocity map and the coregistered vertical magnetogram, respectively. Overall, there is no correlation between $v_{\rm rib}$ and B_z. Negative correlations are only

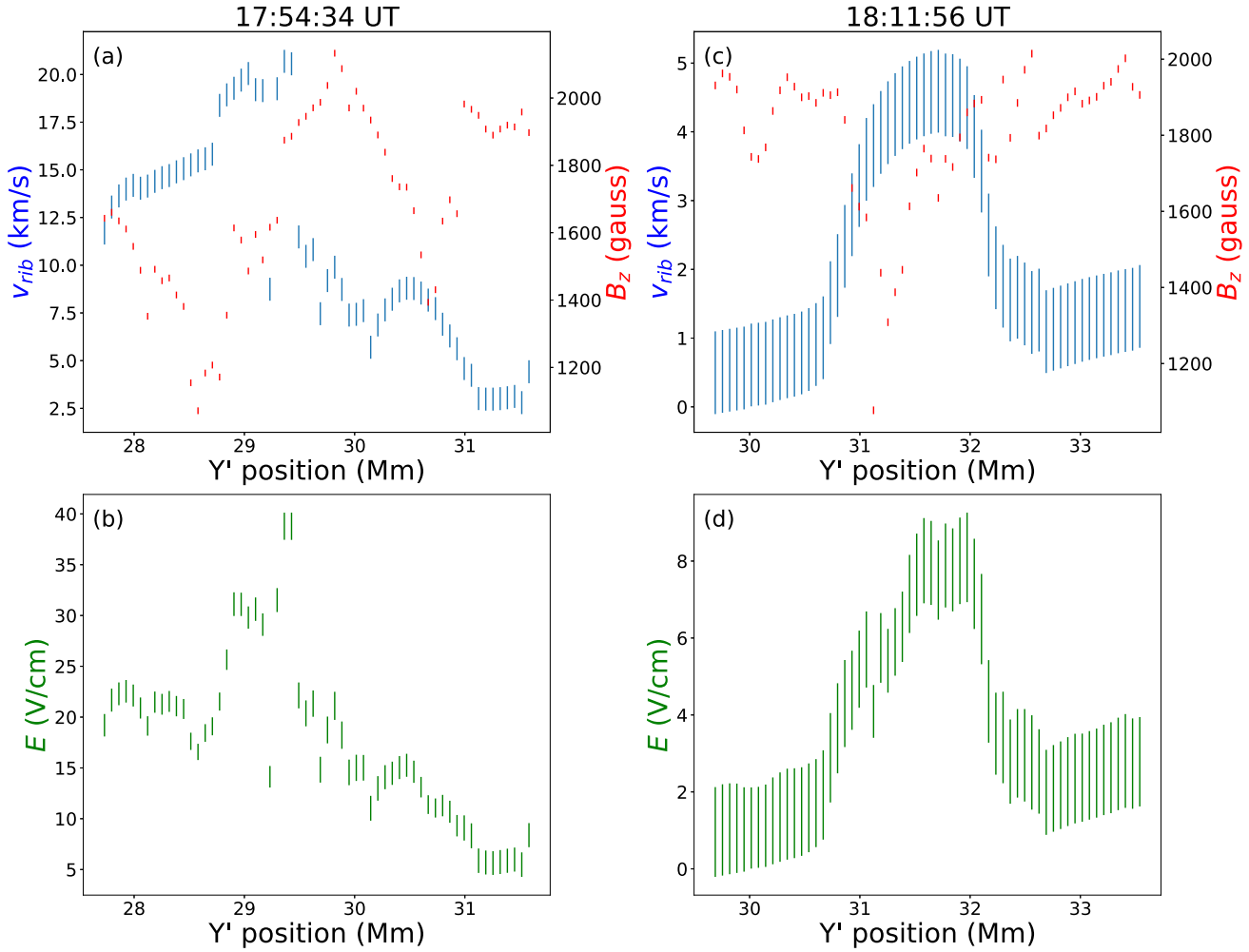

Figure 5. (a) The spatial distribution of $v_{\rm rib}$ (blue) and B_z (red) along the leading edge as a function of position at 17:54:34 UT. When entering the light bridge, the locations of the small magnetic fields tend to coincide with locations of high $v_{\rm rib}$. Error bars for $v_{\rm rib}$ are found by taking one pixel at a time and finding the standard deviation in velocity over time to find a standard deviation map. Then, the spatial average is taken to give the final uncertainty. Uncertainty in B_z is known to be about 10 Gauss. (b) The spatial distribution of reconnection rate E along the leading edge. Error bars are found by adding the relative errors of $v_{\rm rib}$ and B_z. (c) The same as (a), but at 18:11:56 UT when leaving the light bridge. (d) The same as (b), but at 18:11:56 UT.

present at specific locations at specific times. The LB, which is well resolved in the high-resolution of GST data, is one such special region. Figures 4(a) and (b) show $v_{\rm rib}$ vectors along the leading edge of the ribbon at 17:54:34 UT (when the flare ribbon is entering the light bridge) and 18:11:56 UT (when the ribbon is leaving the light bridge), respectively. Figures 4(c) and (d) show the corresponding scatterplots of $v_{\rm rib}$ versus B_z for these two moments. A moderate negative correlation can be identified, with a correlation coefficient of $\sim$0.5.

Such a negative correlation between $v_{\rm rib}$ and B_z is also demonstrated in Figures 5(a) and (c), which show the spatial variation of $v_{\rm rib}$ and B_z along the leading edge of the ribbon at these two moments. The anticorrelation between $v_{\rm rib}$ and B_z is evident. The spatial variation of E, calculated as the product of $v_{\rm rib}$ and B_z, is shown in Figures 5(b) and (d). Although the inhomogeneity of E is somewhat attenuated by the negative correlation between $v_{\rm rib}$ and B_z, the measured E along the ribbon is not uniform. The profile of E is largely determined by that of $v_{\rm rib}$.

To address the spatial properties of magnetic reconnection, we accommodate the inhomogeneous ribbon structure by treating each point at the ribbon front independently of each other, i.e., allowing E to vary along the ribbon axis (y'-axis) as well as the ribbon propagation direction (x'-axis). In this way, we can obtain the spatial distribution of E over the region swept by the ribbon. Figure 6(a) illuminates the spatial distribution of E over the entire region swept over by the ribbon. The value of E at each point is the product of $v_{\rm rib}$ (i.e., v_x obtained by the LCT algorithm) and B_z (read from the magnetogram) at that point, which is a point swept by the ribbon front at a given time. Overall, E is strong near the PIL and gradually decreases as it deviates from the PIL. Since the flare ribbon is a projection of the coronal magnetic reconnection on the chromosphere, the E structure derived from the ribbon morphology and motion can shed light on the reconnecting current sheet in the corona. We then try to compare the obtained E field with the energy deposition rate as indicated by the Ramaty High Energy Solar Spectroscopic Imager (RHESSI) HXR emission. The HXR image is reconstructed using the CLEAN algorithm (Hurford et al. 2003) with RHESSI front detectors 4–8 integrated in the time interval of 18:04:46 UT to 18:05:46 UT. The E field inferred from the ribbon motion is almost continuously distributed, while the HXR emission distribution is much more compact due to the low dynamic range of RHESSI, which may prevent us from seeing the extended ribbon structure beyond the HXR core. Within the FOV of the GST observation, we can

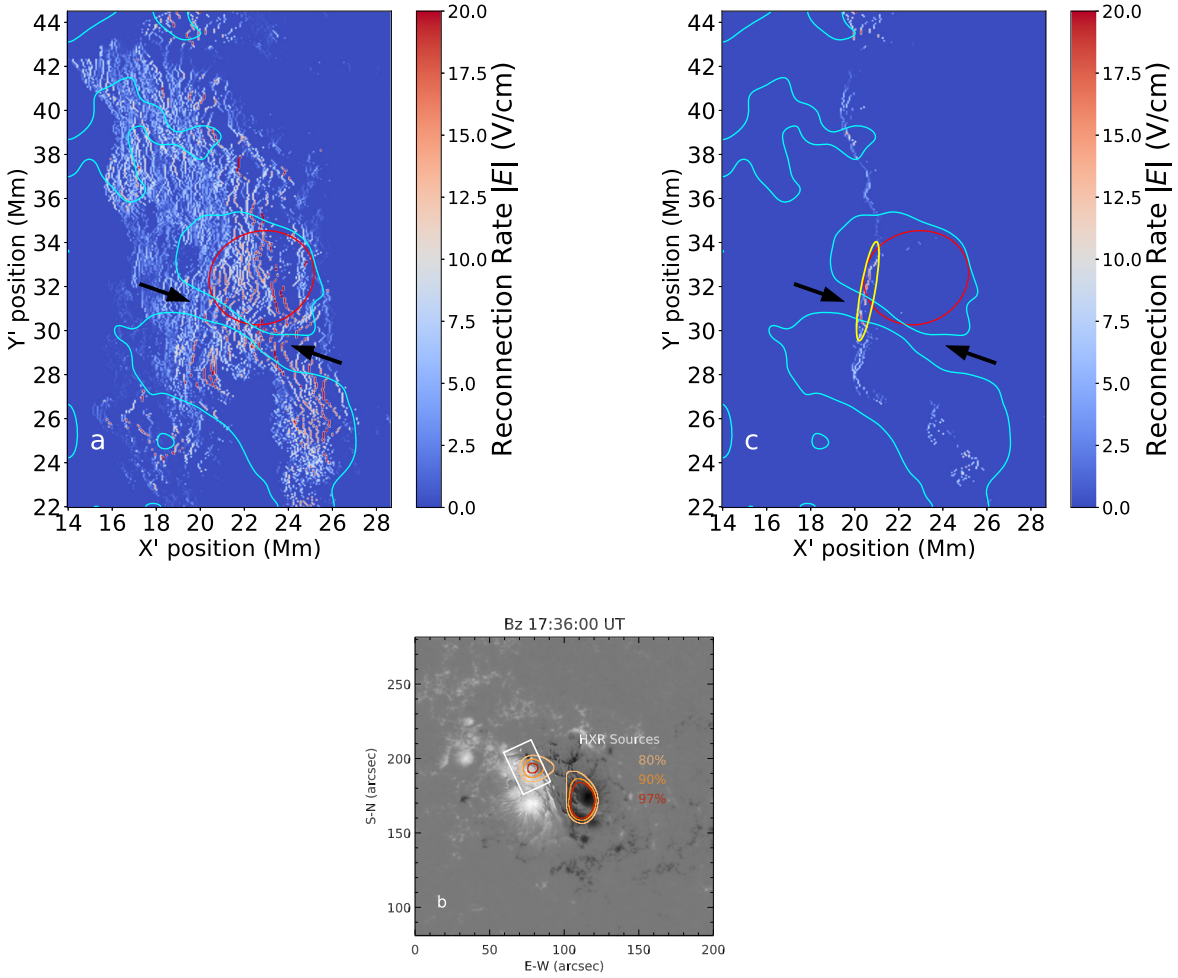

Figure 6. (a) Spatial distribution of the reconnection rate, E, obtained at different times (17:51:14 UT to 18:29:29 UT). The red contour is the RHESSI HXR intensity of 97% of the maximum integrated in the time interval of 18:04:46 to 18:05:46 UT at the 25–50 keV energy range. The blue contours are the 48% maximum of the smoothed GST Hα intensity (taken at 17:36 UT) to outline the sunspots. The two arrows indicate the two ends of the LB located between the two sunspots. The FOV is the same as that in Figure 4(a). (b) HMI magnetogram B_z at 17:36:00 UT, in which the high-resolution NIRIS magnetogram B_z at 17:31:29 UT is embedded, superimposed with contours of 80%, 90%, and 97% of the maximum HXR intensity. The white box shows the FOV of panel (a). (c) Spatial distribution of E, obtained over 18:04:46 UT to 18:05:46 UT when the HXR map is reconstructed. The strongest E is highlighted by the yellow oval.

see one HXR source (outlined in red contour) at the 25–50 keV energy range located near a sunspot in positive polarity. The other HXR footpoint in negative polarity is outside the FOV of the GST images but can be seen in the HMI magnetogram with an expanded FOV (Figure 6(b)). Although the HXR source within the GST's FOV appears in a location where E is relatively strong, there are other locations with strong E but without strong HXR emission. This may be due to the low dynamic range and low resolution of the HXR maps, as well as finite time differences between the E map and the HXR map. The E map is obtained at different times (17:51:14 UT to 18:29:29 UT), while the HXR map is derived at a 1 minute (18:04:46 UT to 18:05:46 UT) integration. We thus plot, in Figure 6(c), only the E distribution over the 1 minute period when the HXR map is reconstructed. During this short period, the strongest E (highlighted with a yellow oval) overlaps with the location of the concentrated HXR source, although the degree of overlapping is compromised by the poor resolution of the HXR map. The average E within the yellow oval is about 7.5 V cm^{-1}, while the average E elsewhere in the ribbon front is ~0.04 V cm^{-1}.

We also calculate the reconnection flux Φ and its change rate $\dot{\Phi}$ for each moment. The latter is another proxy for the coronal reconnection rate in addition to E. $\dot{\Phi}$ is usually used to study the change rate of the reconnection flux, and the measurement of $\dot{\Phi}$ does not depend on the assumption of the 2D configuration, nor on the measurement of any velocity. To derive Φ and $\dot{\Phi}$, we applied the method introduced in Kazachenko et al. (2017) to the time sequence of GST Hα images. The method sums all the newly brightened areas, da, at each moment with respect to the previous moment and integrates the magnetic flux over da. The uncertainty of Φ arises mainly from the varying area measurement, da, and the subsequent $\int B_z da$, the former being obtained by varying the empirical Hα intensity threshold from 1.5 to 2.5 times the median background intensity. The uncertainty of Φ is then divided by the time step Δt to obtain the uncertainty of $\dot{\Phi}$. Since there is a data gap in the RHESSI HXR data between 17:48 UT and 18:04 UT, to compare the temporal variation of $\dot{\Phi}$ with that of the flare nonthermal emission, we use the time derivative of the soft X-ray (SXR) light curve to represent the evolution of the nonthermal emission, known as the Neupert effect (Neupert 1968).

Figure 7 shows the temporal variation of reconnection flux Φ and its change rate $\dot{\Phi}$, in comparison with the GOES SXR light curve and its time derivative, respectively. The GST Hα light curve is also plotted in Figure 7(a) to show how the

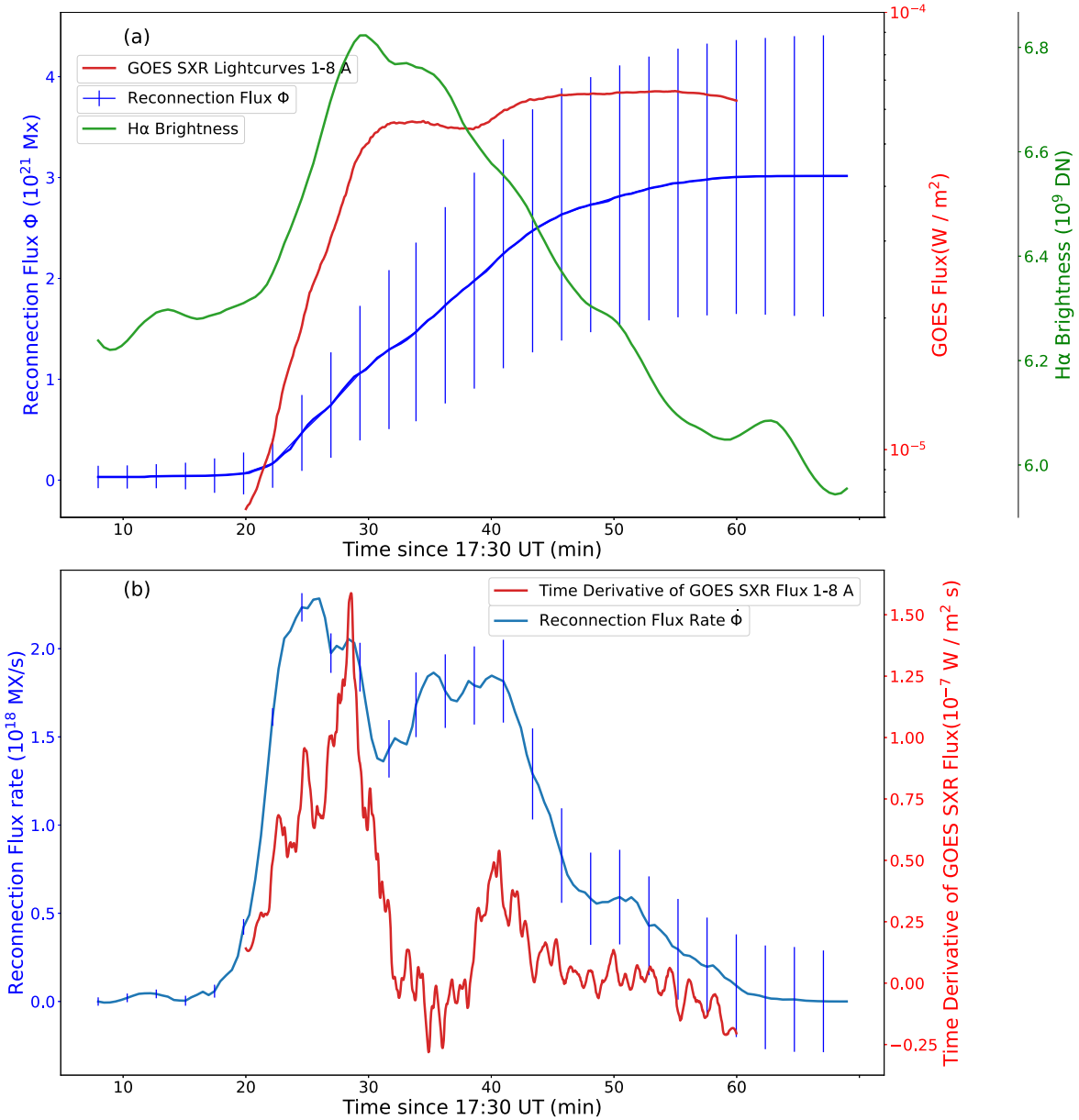

Figure 7. (a) GOES SXR light curve (red), GST Hα lightcurve (green), and the temporal variation of reconnection Flux Φ (blue). (b) Time derivative of GOES SXR light curve (red) and reconnection flux rate $\dot{\Phi}$ (blue). The reconnection flux derivative $\dot{\Phi}$ is smoothed with a 7 minute window.

Hα emission evolves along with the reconnection flux Φ. In general, the time profile of $\dot{\Phi}$ is correlated with the time derivative of the SXR light curve: both exhibit two distinct peaks and reach their maximum at about the same time, demonstrating the relationship between the magnetic reconnection rate and the energy release rate in flares. However, the temporal evolution of $\dot{\Phi}$ and that of the nonthermal emissions are not perfectly synchronized. For example, the first peak of the time derivative of the SXR light curve lags $\dot{\Phi}$ by $\sim$4 minutes. Another example is that at 18:05–18:06 UT, $\dot{\Phi}$ rises to its second peak, while the time derivative of the SXR light curve is at its minimum and reaches its second peak after $\sim$6 minutes. These asynchronous time profiles imply that the nonthermal electron acceleration is delayed relative to the magnetic reconnection. Such a time delay may be explained by a recent finding of 3D MHD simulations that in the presence of a strong guide field, Fermi acceleration of nonthermal electrons can be suppressed (Arnold et al. 2021; Dahlin et al. 2022). In this scenario, if the strong guide field is weakened with time, the nonthermal electron acceleration may appear to be delayed relative to the reconnection, as was indeed noticed in many previous studies (e.g., Jing et al. 2016; Liu et al. 2018; Wang et al. 2018; Sahu et al. 2020; Naus et al. 2022, and references therein). The variation of the guide field in the reconnecting current sheet (RCS) can be inferred from the observed variation of magnetic shear, and the delayed HXR emission, with respect to both the magnetic reconnection rate and magnetic shear, has also been reported in previous studies (Qiu et al. 2010; Qiu & Cheng 2022). In this flare, the magnetic field was highly sheared around the PIL, and thus the guide field was strong at the onset of the flare and then could become weaker as the magnetic fields are progressively unsheared.

5. Summary

Coronal magnetic reconnection rate measurements are envisioned under the standard model of two-ribbon flares. Using high-resolution GST observations, we have analyzed the temporal and spatial variation of the reconnection rate of the M6.5 flare (SOL2015-06-22T18:23).

To summarize, the time derivative of the SXR light curve (a proxy for nonthermal HXR emission) is generally correlated with the reconnection flux change rate in time, albeit with a time delay. Spatially, E is stronger when the ribbon is close to the PIL and decreases as it deviates from the PIL. The HXR emission is concentrated and appears close to a sunspot. At the same time, the strongest E and the concentrated HXR source show a spatial correlation. The temporal and spatial correlations between the reconnection rate and high-energy flare radiation found in many earlier studies (e.g., Qiu et al. 2002, 2004, 2010; Lee et al. 2006) and in this study are considered an important piece of evidence for the standard reconnection model.

We also investigated the relationship between the ribbon speed, $v_{\rm rib}$, and the vertical field strength, B_z, at the location encountered by the ribbon front. Overall, $v_{\rm rib}$ and B_z are not correlated with each other, and the spatial distribution of E is largely determined by that of $v_{\rm rib}$ but not that of B_z. The same trend was reported by Lee et al. (2006) who studied one-dimensional ribbon motion by reducing an Hα ribbon to a center-of-mass point. In the present study, we studied the ribbon dynamics in two dimensions as is. As a result, not only temporal but spatial correlation between the ribbon motion and the HXR emission was found, by which we could distinguish between the contribution of $v_{\rm rib}$ and that of B_z to E using high-resolution observation. According to the present result, the spatially and temporally varying ribbon motion reflects that the coronal electric field is neither spatially uniform nor temporally constant.

In particular, the leading edge of the ribbon entering and exiting the LB runs ahead of the rest of the ribbon (indicated by the white arrow in Figure 2(b) as an example) where local B_z is low. As a comparison, Asai et al. (2004) suggested a scaling law of $v_{\rm in}$ with B_c in the corona either for the Sweet–Parker mechanism (Parker 1957; Sweet 1958) or for the Petschek mechanism (Petschek 1964). This scaling law, if the ratio of B_c to B_z is the same all over the flare region, predicts a positive correlation between $v_{\rm rib}$ and B_z in the photosphere. Our finding of the weak or negative correlations of $v_{\rm rib}$ with B_z implies that such a scaling law of reconnection inflow speed may not be universal.

Another finding of the present high-resolution observation is the fine structure of the ribbon in the form of whirls or hooks, which is particularly evident when the ribbon leaves the LB. Such features may indicate the influence of turbulence in the coronal current sheet on reconnection, as demonstrated by recent high-resolution MHD simulations by Wyper & Pontin (2021) and Dahlin et al. (2021). According to the simulation results, most of the ribbon fine structures originate from the tearing mode and are linked to the formation of magnetic islands within the reconnecting current sheet.

Acknowledgements

We would like to thank Dr. Joel T. Dahlin for providing information that helped us understand the cause of the delay in nonthermal electron acceleration relative to reconnection. We gratefully acknowledge the use of data from the Goode Solar Telescope (GST) of the Big Bear Solar Observatory (BBSO). BBSO operation is supported by US NSF AGS-2309939 and AGS-1821294 grants and New Jersey Institute of Technology. GST operation is partly supported by the Korea Astronomy and Space Science Institute and the Seoul National University. B.C., J.J., Q.L., N.L., J.L., W.C., and H.W. were supported by NASA grants 80NSSC23K0406, 80NSSC21K1671, 80NSSC21K0003, 80NSSC20K0025, 80NSSC19K0068, 80NSSC19K0257, and 80NSSC19K0859, and NSF grants AGS 1927578, 1954737, 2114201, 2149748, AST 2206424, 2108235, and 2309939.

ORCID iDs

Ju Jing https://orcid.org/0000-0002-8179-3625
Nian Liu https://orcid.org/0000-0002-6018-3799
Jeongwoo Lee https://orcid.org/0000-0002-5865-7924
Wenda Cao https://orcid.org/0000-0003-2427-6047
Haimin Wang https://orcid.org/0000-0002-5233-565X

References

Ahn, K., & Cao, W. 2017, AAS/SPD Meeting, 48, 115.04
Ahn, K., Cao, W., Shumko, S., & Chae, J. 2016, AAS/SPD Meeting, 47, 2.07
Arnold, H., Drake, J. F., Swisdak, M., et al. 2021, PhRvL, 126, 135101
Asai, A., Yokoyama, T., Shimojo, M., et al. 2004, ApJ, 611, 557
Brannon, S. R., Longcope, D. W., & Qiu, J. 2015, ApJ, 810, 4
Cao, W., Goode, P. R., Ahn, K., et al. 2012, in ASP Conf. Ser. 463, Second ATST-EAST Meeting: Magnetic Fields from the Photosphere to the Corona, ed. T. R. Rimmele et al. (San Francisco, CA: ASP), 291
Cao, W., Gorceix, N., Coulter, R., et al. 2010, AN, 331, 636
Carmichael, H. 1964, in The Physics of Solar Flares, Vol. 50 ed. W. N Hess (Washington, DC: NASA), 451
Dahlin, J., Antiochos, S., Qiu, J., DeVore, C., & Wyper, P. 2021, BAAS, 53, 127.10
Dahlin, J. T., Antiochos, S. K., Qiu, J., & DeVore, C. R. 2022, ApJ, 932, 94
Fisher, G. H., & Welsch, B. T. 2008, in ASP Conf. Ser. 383: Subsurface and Atmospheric Influences on Solar Activity, ed. R. Howe et al. (San Francisco, CA: ASP), 373
Forbes, T., & Priest, E. 1984, SoPh, 94, 315
Gary, G. A., & Hagyard, M. J. 1990, SoPh, 126, 21
Goode, P. R., & Cao, W. 2012, Proc. SPIE, 8444, 844403
Hirayama, T. 1974, SoPh, 34, 323
Huang, N., Xu, Y., Sadykov, V. M., Jing, J., & Wang, H. 2019, ApJL, 878, L15
Hurford, G. J., Schmahl, E. J., Schwartz, R. A., et al. 2003, in The Reuven Rhamaty High-Energy Solar Spectroscopic Imager (RHESSI), ed. R. P. Lin (Dordrecht: Springer), 61
Jing, J., Chae, J., & Wang, H. 2008, ApJL, 672, L73
Jing, J., Qiu, J., & Lin, J. 2005, ApJ, 620, 1085
Jing, J., Xu, Y., Cao, W., et al. 2016, NatSR, 6, 24319
Kazachenko, M. D., Lynch, B. J., Welsch, B. T., & Sun, X. 2017, ApJ, 845, 49
Kopp, R., & Pneuman, G. 1976, SoPh, 50, 85
Lee, J. 2015, JASS, 32, 101
Lee, J., Gary, D. E., & Choe, G. 2006, ApJ, 647, 638
Leka, K. D., Barnes, G., & Crouch, A. 2009, in ASP Conf. Ser. 415, The Second Hinode Science Meeting: Beyond Discovery-Toward Understanding, ed. B. Lites et al. (San Francisco, CA: ASP), 365
Liu, C., Cao, W., Chae, J., et al. 2018, ApJ, 869, 21
Liu, C., Lee, J., Gary, D. E., & Wang, H. 2007, ApJL, 658, L127
Liu, C., Xu, Y., Cao, W., et al. 2016, NatCo, 7, 13104
Metcalf, T. R. 1994, SoPh, 155, 235
Metcalf, T. R., Leka, K. D., Barnes, G., et al. 2006, SoPh, 237, 267
Naus, S. J., Qiu, J., DeVore, C. R., et al. 2022, ApJ, 926, 218
Neupert, W. M. 1968, ApJL, 153, L59
Parker, E. N. 1957, JGR, 62, 509
Petschek, H. E. 1964, in AAS-NASA Symp.: The Physics of Solar Flares, ed. W. N. Hess (Washington, D.C.: Scientific and Technical Information Division, National Aeronautics and Space Administration), 425
Qiu, J., & Cheng, J. 2022, SoPh, 297, 80

Qiu, J., Lee, J., Gary, D. E., & Wang, H. 2002, ApJ, 565, 1335
Qiu, J., Liu, W., Hill, N., & Kazachenko, M. 2010, ApJ, 725, 319
Qiu, J., Wang, H., Cheng, C., & Gary, D. E. 2004, ApJ, 604, 900
Sahu, S., Joshi, B., Mitra, P. K., Veronig, A. M., & Yurchyshyn, V. 2020, ApJ, 897, 157
Sturrock, P. 1966, Natur, 211, 695
Sweet, P. A. 1958, in IAU Symp. 6, Electromagnetic Phenomena in Cosmical Physics, ed. B. Lehnert (Cambridge: Cambridge Univ. Press), 123
Wang, H., Liu, C., Ahn, K., et al. 2017, NatAs, 1, 0085
Wang, J., Liu, C., Deng, N., & Wang, H. 2018, ApJ, 853, 143
Wyper, P. F., & Pontin, D. I. 2014, PhPl, 21, 102102
Wyper, P. F., & Pontin, D. I. 2021, ApJ, 920, 102
Xu, Y., Cao, W., Ahn, K., et al. 2018, NatCo, 9, 46
Xu, Z., Baojie, X., & Guoxin, W. 2017, in IEEE Int. Conf. 13, Electronic Measurement and Instruments, (ICEMI) (IEEE), 53
Zhu, C., Qiu, J., Liewer, P., et al. 2020, ApJ, 893, 141